Flux penetration into flat rectangular superconductors with anisotropic critical current

Th. Schuster, H. Kuhn, and E. H. Brandt

Max-Planck-Institut für Metallforschung, Postfach 800665, D-70506 Stuttgart, Germany

S. Klaumünzer

Hahn-Meitner-Institut, Postfach 390128, D-14091 Berlin, Germany

(Received 16 January 1997)

Superconductors with anisotropic critical-current density j_c exhibit characteristic anisotropic flux-density patterns during penetration of magnetic flux. We investigate this anisotropic flux penetration in detail by observations using the magneto-optical Faraday effect and by first-principles calculations which describe the superconductor as a nonlinear anisotropic conductor. Our samples are thin plates of $DyBa_2Cu_3O_{7-\delta}$ into which anisotropic pinning is introduced by oblique irradiation with 340-MeV Xe ions creating linear defects. Excellent agreement between experiment and theory is obtained. In particular, we find that in rectangular plates with j_c anisotropy equal to the side ratio, the intrinsic and shape anisotropies may *compensate* such that the flux pattern looks like that in an isotropic square stretched to the rectangular shape. This means the current streamlines are concentric rectangles which shrink to a point rather than to a line, and the discontinuity lines where the current bends sharply, coincide with the diagonals of the rectangle rather than forming the usual double-Y structure. [S0163-1829(97)08330-6]

I. INTRODUCTION

Since the discovery of high-temperature superconductors (HTSC's) a great deal of effort has been made to investigate the influence of their strong anisotropy on their superconducting properties. The reported anisotropy of the superconducting order parameter in the *a-b* plane especially stimulated the still ongoing discussion about *s*- and *d*-wave superconductivity. However, many features which are important for applications are sufficiently characterized by *macroscopic* quantities like the critical-current density j_c and the activation energy U. When the supercurrents reach j_c, the vortices depin and start to move under the influence of the Lorentz force. This vortex drift induces an electric field E which causes a voltage drop along the specimen. Energy is thus dissipated at large current densities $j > j_c$ where the resistivity $\rho = E/j$ becomes finite. In HTSC's the vortices may also depin at low current densities $j \ll j_c$ by thermally activated depinning, which is characterized by an activation energy U.

The strong dependence of nearly all physical quantities of the HTSC's on the crystalline orientation results from their orthorhombic crystal structure, which leads to anisotropic electronic properties both in planes parallel and perpendicular to the crystalline *c* axis. Since superconductivity takes place mainly perpendicular to the *c* axis, in the Cu-O planes, j_c is typically much larger in the *a-b* plane than parallel to the *c* axis. An informative method for investigating anisotropic current distributions is the observation of the penetration of magnetic flux with high spatial resolution when an external magnetic field is applied.

Flux penetration into type-II superconductors with flux-line pinning is well described by the Bean model[1] and its extensions[2–6] in the case of infinitely extended cylinders or slabs with constant j_c in a parallel magnetic field where demagnetizing effects are negligible. The introduction of a de-

magnetizing factor accounts for these effects only in the case of ellipsoidal samples without pinning (linear response). However, monocrystalline HTSC samples are available only as thin films or monocrystalline platelets, which are usually investigated in a perpendicular magnetic field to produce larger signals. In this geometry one has to account for large stray-field effects, and the original Bean model can be applied only to the *critical state*, in which the sample is completely penetrated by magnetic flux and the shielding current has reached the critical value j_c in the entire superconductor.[7] Forkl and Kronmüller[8] successfully used the Bean model to describe magneto-optically observed flux-density profiles at the flat surface of samples with finite thickness in the critical state. The description of flux and current distributions in the *partly penetrated* state is much more complicated. A numerical method to calculate the current distribution in thin circular disks from measured flux-density profiles was reported by Theuss *et al.*[9]

Analytic expressions for the static magnetization and for flux and current profiles during flux penetration and exit are available for the one-dimensional (1D) perpendicular Bean model of long strips[10–12] and circular disks[13–15] and for thin strips with a geometric edge barrier.[16,17] These 1D theories of thin long strips and circular disks have recently been extended to the two-dimensional (2D) problems of thin superconductors with square, rectangular or arbitrary shape in a perpendicular field.[18–20] Recent magneto-optical studies[21–25] demonstrate that the flux penetration and exit and the flux creep are well described by model calculations using a current-voltage law, e.g., of the form $E \propto (j/j_c)^n$, which conveniently interpolates between the Ohmic regime of thermally activated flux flow ($n = 1$) and the classical Bean model ($n \gg 1$). Here E is the electric field and the exponent n is determined by the activation energy U. The often observed dependence $U(j) = U_c \ln(j_c/j)$ indeed yields such a power law $E(j) = E_c \exp(-U/kT) = E_c(j/j_c)^n$ with $n = U_c/kT$.

The current distribution was calculated for thin rectangular specimens from this model in Refs. 18 and 24 and nice agreement with the observed cushionlike flux penetration was obtained. The electric field E was found to be maximum along the boundaries where j_c changes abruptly[24] in samples with inhomogeneous critical-current density $j_c(\mathbf{r})$. A strong enhancement of the electric field occurs at concave sample corners, which even becomes infinite when the corners are sharp.[25]

In this paper we present an extension of the above isotropic theory to samples with anisotropic critical-current density. The obtained flux patterns are compared with magneto-optically determined field distributions of samples in which an anisotropy of j_c in the a-b plane was induced by crossed linear defects (LD's) introduced by high-energy heavy-ion irradiation.[26,27] Since samples with the c axis lying in the plane of observation mostly exhibit macrodefects which disturb the magneto-optically visualized flux patterns,[28–30] we investigate here features of the anisotropic critical current in HTSC's with irradiation-induced anisotropy rather than in samples with a natural critical-current anisotropy caused by intrinsic flux-line pinning at Cu-O planes.

This paper is organized as follows. The main equations used for the calculations are given in Sec. II together with typical results for the current stream lines and profiles of the magnetic and electric fields during flux penetration into quadratic and rectangular films with isotropic and anisotropic critical-current density. In Sec. III our magneto-optical method and sample preparation are described, and the observed pictures of flux penetration into anisotropic films are presented. Finally, our theoretical and experimental results are discussed and summarized in Sec. IV.

II. THEORY

A. Critical state in rectangular superconductors

Our computation reproduces the results of the Bean model for the particular choices $j_c(H) =$ const and $n \gg 1$ in $E(j) = E_c(j/j_c)^n$. The current density attains its maximum possible value $j = |\mathbf{j}| = j_c$ in the entire specimen when the sample is in the critical state, i.e., fully penetrated by magnetic flux. In addition, the current density has to satisfy the continuity condition div$\mathbf{j} = 0$ and has to flow parallel to the surfaces. It follows from these conditions that the current stream lines have sharp bends in superconductors with rectangular cross section; this is a characteristic feature of vector fields with constant modulus.[31] These sharp bends form discontinuity lines (d lines) which divide the superconductor into domains with uniform parallel current flow as discussed in the review by Campbell and Evetts;[2] see the upper plot in Fig. 1. One distinguishes two types of d lines:[7] At d^+ lines the orientation of $\mathbf{j}_c$ changes discontinuously but the magnitude of j_c remains the same. At d^- lines the magnitude of j_c changes, e.g., at the specimen surface or at inner boundaries where regions of different j_c meet. The current stream lines have to bend sharply in the critical state in order to satisfy the condition of continuous current flow at such boundaries. The d^+ lines run along the bisection lines starting from the sample corners and on a section of the central line parallel to the longer side as shown in the lower plot in Fig. 1, when the superconductor is isotropic in the x-y plane.
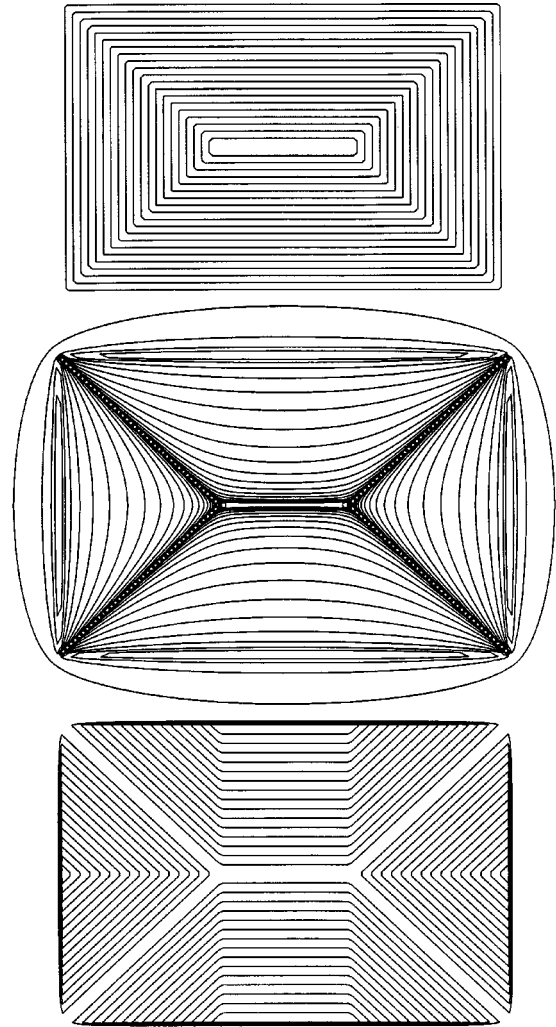

FIG. 1. Top: Stream lines of the current in a thin type-II superconductor of rectangular shape in the critical state. Middle: Contour plot of the normal component of the magnetic field in and around the rectangle. Bottom: Contour plot of the magnitude of the electric field inside the rectangle during field ramping in the critical state.

Characteristic features of the d^+ and d^- lines are the following.

(1) Whereas the d^- lines occur at internal and external boundaries of the sample (local sample geometry), the d^+ lines form in homogeneous regions and are determined by the shape of the sample.

(2) Flux lines cannot cross the d^+ lines since during increase or decrease of the applied magnetic field the flux motion is directed towards or away from the d^+ lines, respectively. In contrast, the d^- lines can be crossed by moving flux lines, e.g., when flux lines penetrate from the surface. When the current does not flow parallel to the d^- line, a strong flux motion is directed along the d^- line.

(3) The electric field E is largest at the d^- lines, whereas we have $E = 0$ at the d^+ lines.[24,19]

(4) The d^+ and the d^- lines do not change their position during lowering or reversal of the external magnetic field, although the magneto-optically detected intensities of the d^+ and d^- lines are reversed in the remanent state.

The d^+ and d^- lines are clearly seen in thin type-II superconductors (thickness $\ll$ lateral extension) because of the logarithmic infinity of B_z at the sample surface.[7]

B. Basic equations

The equation of motion for the sheet current $\mathbf{J}(x,y,t)=\mathbf{j}d$ in a thin planar conductor or superconductor of thickness d and arbitrary shape in a perpendicular field $\hat{\mathbf{z}}H_a(t)$ is derived in the following way.[18–20,24] We characterize the material by $\mathbf{B}=\mu_0\mathbf{H}$ and by a resistivity $\rho=E/j$ or sheet resistivity $\rho_s=E/J=\rho/d$, which may be nonlinear, e.g., $\rho(j)=\rho_c(j/j_c)^{n-1}$, or linear, complex, and frequency dependent, $\rho=\rho_{ac}(\omega)=\rho'+i\rho''$. The sheet resistivity $\rho_s(x,y)$ may depend on the position $\mathbf{r}$ either directly (in a nonuniform specimen) or implicitly via $J(x,y)$ and $B_z(x,y)$.

Planar anisotropy of the resistivity $\rho(j)$, which becomes now a tensor, can be incorporated into this theory if the resistivity is linear or if the currents mainly flow along the principal axes of the anisotropy. The latter condition is satisfied in homogeneous superconductors with the shape of a rectangle with its edges along the anisotropy axes if the resistivity is highly nonlinear, i.e., in the Bean-like case. One should note that a more general theory for ''arbitrary nonlinear and anisotropic resistivity'' presents fundamental difficulties.[32] As shown by Gurevich[33,34] the assumption of general anisotropic nonlinear resistivity may lead to an instability of the current flow and to a spontaneous creation of cells of circular currents (''macroturbulence'').

To obtain this equation of motion one first expresses the sheet current by a scalar function $g(x,y)$ as

$$\mathbf{J}(x,y)=-\hat{\mathbf{z}}\times\nabla g(x,y)=\nabla\times\hat{\mathbf{z}}g(x,y). \qquad (1)$$

This substitution guarantees that $\text{div}\mathbf{J}=0$ and that the current flows along the specimen boundary if one sets $g(x,y)=\text{const}=0$ there. In general, the lines $g(x,y)=\text{const}$ coincide with the current stream lines. The physical meaning of $g(x,y)$ is the local magnetization or density of tiny current loops. Thus, the integral of $g(x,y)$ over the specimen area yields the magnetic moment

$$\mathbf{m}=\frac{1}{2}\int \mathbf{r}\times\mathbf{J}(\mathbf{r})d^2r=\hat{\mathbf{z}}\int g(\mathbf{r})d^2r. \qquad (2)$$

Next, one determines the integral kernel $Q(\mathbf{r},\mathbf{r}')$ ($\mathbf{r}=x,y$) which relates the perpendicular field $H_z(x,y)$ in the specimen plane $z=0$ to $g(x,y)$ by

$$H_z(\mathbf{r})=H_a+\int_A Q(\mathbf{r},\mathbf{r}')g(\mathbf{r}')d^2r'. \qquad (3)$$

This may be inverted to give

$$g(\mathbf{r})=\int_A Q^{-1}(\mathbf{r},\mathbf{r}')[H_z(\mathbf{r}')-H_a]d^2r'. \qquad (4)$$

The integrals in Eqs. (2) and (3) are over the specimen area A and Q^{-1} is the inverse kernel of Q, defined by $\int_A Q^{-1}(\mathbf{r},\mathbf{r}'')Q(\mathbf{r}'',\mathbf{r}')d^2r''=\delta(\mathbf{r}-\mathbf{r}')$.

Finding the 2D integral kernel Q is not a trivial task, since when one performs the limit of zero thickness in the Biot-Savart law, the kernel becomes highly singular, $Q=-1/4\pi|\mathbf{r}-\mathbf{r}'|^3$; this form of the kernel thus applies only when $\mathbf{r}$ lies *outside* the specimen, but *inside* the specimen area (where $\mathbf{r}=\mathbf{r}'$ can occur) one should perform part of the

integration (3) analytically to obtain a well-behaved kernel as described in Ref. 35. Alternatively, one may obtain this kernel numerically for a small but finite height z above the specimen.[36,37] Knowing that the field of a tiny current loop (or magnetic dipole) of unit strength located at $x=y=z=0$ with axis along z is $H_z(x,y,z)=(1/4\pi)(2z^2-x^2-y^2)/(x^2+y^2+z^2)^{5/2}$, one obtains for the kernel (still for arbitrary shape of the thin plate)

$$Q(\mathbf{r},\mathbf{r}')=\frac{1}{4\pi}\lim_{z\to 0}\frac{2z^2-\rho^2}{(z^2+\rho^2)^{5/2}} \qquad (5)$$

with $\rho^2=(x-x')^2+(y-y')^2$. From Q Eq. (5) the inverse kernel Q^{-1} may be obtained by Fourier transform or by introducing a grid with positions $\mathbf{r}_i=(x_i,y_i)$ and weights w_i, the vectors $H_i-H_a=H_z(\mathbf{r}_i)$ and $g_i=g(\mathbf{r}_i)$, and the matrix $Q_{ij}=Q(\mathbf{r}_i,\mathbf{r}_j)w_j$. The integrals (3) and (4) then are approximated by the sums $H_i=\Sigma_j Q_{ij}g_j$ and $g_i=\Sigma_j Q_{ij}^{-1}(H_j-H_a)$ where Q_{ij}^{-1} is the inverse matrix of Q_{ij} as described in the Appendix of Ref. 19.

As the last step, the equation of motion for $g(x,y,t)$ is obtained from the 3D induction law $\nabla\times\mathbf{E}=-\dot{\mathbf{B}}$ and from the material laws $\mathbf{B}=\mu_0\mathbf{H}$ and $\mathbf{E}=\rho\mathbf{j}$, valid inside the sample where $\mathbf{j}=\mathbf{J}/d=-\hat{\mathbf{z}}\times(\nabla g)/d$. Note that the required z component $\dot{B}_z=\hat{\mathbf{z}}\dot{\mathbf{B}}=-\hat{\mathbf{z}}(\nabla\times\mathbf{E})=-(\hat{\mathbf{z}}\times\nabla)\mathbf{E}=-\hat{\mathbf{x}}\partial\mathbf{E}/\partial y+\hat{\mathbf{y}}\partial\mathbf{E}/\partial x$ does not depend on the (unknown) derivative $\partial\mathbf{E}/\partial z$. With $\rho_s=\rho/d$ one may write inside the sample $\mathbf{E}=\rho\mathbf{j}=\rho_s\mathbf{J}=-\rho_s\hat{\mathbf{z}}\times\nabla g$ and thus $\dot{B}_z=(\hat{\mathbf{z}}\times\nabla)(\rho_s\hat{\mathbf{z}}\times\nabla g)=\nabla\cdot(\rho_s\nabla g)$. Inserting this into Eq. (4) one obtains the equation of motion for $g(x,y,t)$ in the form[18–20,24]

$$\dot{g}(\mathbf{r},t)=\int Q^{-1}(\mathbf{r},\mathbf{r}')[f(\mathbf{r}',t)-\dot{H}_a(t)]d^2r'. \qquad (6)$$

For isotropic $\rho(j)$ the integrand in Eq. (6) is

$$f(\mathbf{r},t)=\nabla\cdot(D_s\nabla g), \qquad (7)$$

with $D_s=\rho_s/\mu_0=\rho/d\mu_0$ the sheet diffusivity of flux. Equations (6) and (7) describe the two-dimensional diffusion of magnetic flux. In the present perpendicular geometry, the diffusion is *nonlocal*, characterized by the integral kernel $Q^{-1}(\mathbf{r},\mathbf{r}')$. In the simpler parallel geometry the flux diffusion is local, obeying a differential equation, since the kernel Q formally reduces to a delta function $\delta(\mathbf{r}-\mathbf{r}')$ times the specimen thickness d, and $g(\mathbf{r})$ then coincides with $H_z(\mathbf{r})-H_a$.[19] In general the diffusion is *nonlinear* and inhomogeneous since the flux diffusivity ρ/μ_0 may depend on $\mathbf{r}$, $\mathbf{J}$, and H_z.

When the resistivity is anisotropic, expressed by the two functions $\rho_{xx}=E_x/J_x$ and $\rho_{yy}=E_y/J_y$, Eq. (6) still applies but with a modified integrand f,

$$f(\mathbf{r},t)=\nabla_x[(\rho_{yy}/d)\nabla_x g]+\nabla_y[(\rho_{xx}/d)\nabla_y g]. \qquad (8)$$

One can show that in the limit of a long strip or of a rectangle with extreme anisotropy $\rho_{xx}\gg\rho_{yy}$ the 2D Eq. (8) reduces to the corresponding 1D expression $f(x,t)$ for an infinitely long strip.[24]

C. Rectangular films and plates

In films or plates with rectangular shape, the boundary condition that $\mathbf{J}$ cannot cross the specimen boundary may be satisfied by expressing $g(x,y)$ as a 2D Fourier series in which each term vanishes at the edges. For a rectangle filling the area $0 \leq x \leq 2a$, $0 \leq y \leq 2b$ one writes[18]

$$g(x,y,t) = \sum_{\mathbf{K}} g_{\mathbf{K}}(t) \sin K_x x \sin K_y y, \qquad (9)$$

where the $\mathbf{K}$ are reciprocal-lattice vectors with the components $K_x = (2m-1)\pi/2a$ and $K_y = (2n-1)\pi/2b$, $m, n = 1, 2, 3, \ldots$. The sum $\Sigma_{\mathbf{K}}$ is over all $m \geq 1$, $n \geq 1$. A similar Fourier series may be written for the field H_z inside the specimen area,

$$H_z(x,y,t) = \sum_{\mathbf{K}} H_{\mathbf{K}}(t) \sin K_x x \sin K_y y. \qquad (10)$$

From Eqs. (2), (9), and (10) one obtains

$$H_{\mathbf{K}}(t) = \sum_{\mathbf{K}'} Q_{\mathbf{K}\mathbf{K}'} g_{\mathbf{K}'}(t), \qquad (11)$$

where the $Q_{\mathbf{K}\mathbf{K}'}$ are the 2D Fourier coefficients of the integral kernel Q in Eq. (2),

$$Q(\mathbf{r},\mathbf{r}') = \frac{1}{ab} \sum_{\mathbf{K}\mathbf{K}'} Q_{\mathbf{K}\mathbf{K}'} \sin K_x x \sin K_y y \sin K_x' x' \sin K_y' y'. \qquad (12)$$

Explicitly one finds from Eqs. (4) and (12) (Refs. 18,19)

$$Q_{\mathbf{K}\mathbf{K}'} = \frac{2}{\pi^2 ab} \int_0^\infty dk_x \frac{K_x K_x'(1 + \cos 2ak_x)}{(k_x^2 - K_x^2)(k_x^2 - K'_x 2)}$$

$$\times \int_0^\infty dk_y k \frac{K_y K_y'(1 + \cos 2bk_y)}{(k_y^2 - K_y^2)(k_y^2 - K_y'^2)}. \qquad (13)$$

Inspection reveals that the integrand in Eq. (13) is sharply peaked at $K_x = K_x'$ and $K_y = K_y'$. In fact, without the common factor $k = (k_x^2 + k_y^2)^{1/2}$ the double integral (13) would separate and would exactly equal $\frac{1}{2}\delta_{\mathbf{K}\mathbf{K}'}$. Therefore, at large K or K' one approximately has $Q_{\mathbf{K}\mathbf{K}'} = \delta_{\mathbf{K}\mathbf{K}'} K/2$. This useful approximation allows us to write the inverse kernel explicitly as $Q_{\mathbf{K}\mathbf{K}'}^{-1} = \delta_{\mathbf{K}\mathbf{K}'} 2/K$ and to obtain approximate analytic expressions.

For rectangular plates or films in increasing, constant, or cycled applied perpendicular field $H_a(t)$, the magnetization $g(x,y,t)$ may be computed by time-integrating the nonlocal diffusion equation (6) with the kernel Q Eqs. (12), (13) and a material law $E = E(j)$, or two laws $E_x(j_x)$ and $E_y(j_y)$ inserted in Eqs. (7) or (8). From $g(x,y,t)$ one obtains the sheet current $\mathbf{J} = \mathbf{j}d = -\hat{\mathbf{z}} \times \nabla g$, the magnetic-field components at the specimen surface H_z Eq. (3), $H_x = J_y/2$, $H_y = -J_x/2$, and the electric field $\mathbf{E} = E(J/d)\hat{\mathbf{J}}$.

D. Nonlinear resistivity and scaling

In this paper we model the anisotropic pinning by two critical sheet current densities J_c^a and J_c^b which enter the nonlinear resistivities $\rho_{xx} = E_x/J_x = (E_c/J_x)|J_x/J_c^a|^n$ and $\rho_{yy} = E_y/J_y = (E_c/J_y)|J_y/J_c^b|^n$ if the anisotropy axes are $a\|x$ and $b\|y$. Throughout this paper we use a constant creep exponent $n = 19$, and constant $J_c = j_c d$ values, though our computational method, in principle, allows for arbitrary dependences of $n(B)$ and $J_c(B)$ on the perpendicular component of the induction $B = \mu_0 H$. For convenience we use the specimen half width a and the critical sheet current J_c^a as units of length and magnetic field. We further set $E_c = 1$ and the ramp rate $\mu_0 \dot{H}_a = \dot{B}_a = 1$, which in real units means $\dot{B}_a = E_c/a$ and a time unit $\tau = \mu_0 J_c^a a/E_c$. In these units, the field of full penetration H_p, which logarithmically depends on the specimen thickness d or on our grid spacing, is $H_p \approx 1.0$. For a thin strip of width $2a \gg d$ one has[45,38,39] $H_p = (J_c/\pi)[1 + \ln(2a/d)]$.

Due to our large creep exponent $n = 19$, which yields an almost creep-free Bean-like example, the chosen ramp rate is not very relevant here. In fact, one can make the following useful statement. Any choice of the ramp rate is equivalent and does not restrict the generality of the computation: Choosing the ramp rate larger by a factor of A (say $A = 10$) would yield identical results except that the obtained $B(\mathbf{r},t)$ and $J(\mathbf{r},t)$ are larger by a constant factor $A^{1/n}$ (here $A^{1/n} = 10^{1/19} = 1.13$) and the time runs faster by a factor $A^{1-1/n}$ (here $10^{18/19} = 8.86$). This scaling law is derived and discussed in more detail in Ref. 38. It applies to any power law $E \propto J^n$ and states that the equations and their solutions remain unchanged if one simultaneously changes the time scale by a factor of $1/C$ (or the frequency scale by a factor of C) and the field and current units by a factor of $C^{1/(n-1)}$.

E. Sheet current and flux density

Figures 2–5 show the computed flux penetration into squares $(b/a = 1)$ and rectangles $(b/a = 1.4)$ of superconductors with isotropic $(J_c^b/J_c^a = 1)$ and anisotropic $(J_c^b/J_c^a = 1.4)$ pinning at three values of the applied field H_a. Note the qualitative similarities of the current stream lines and contour lines of the magnetic field for the isotropic rectangle and anisotropic square, and for the anisotropic rectangle and the isotropic square, respectively. The depicted three states of penetration correspond to $H_a/J_c^a = 0.25$, 0.55, and 1.55 (top to bottom); in the latter case the penetration is complete. We used an exponent $n = 19$ and grids of $N_x \times N_y = 25 \times 25$ (30×22, 22×30, and 25×25) equidistant points, chosen such that in the fully penetrated (critical state) all discontinuity lines run through grid points; this grid choice strongly reduces the numerical noise, in particular of the electric field $E = J^n$. Note that the sheet current is finite over the entire specimen area, even in regions where the perpendicular flux has not yet penetrated.

More detailed three-dimensional computations[39] accounting for the finite thickness d of the superconductor reveal that in the penetrated regions ($B_z \neq 0$) the current density j is constant over the entire thickness, with value j_c, thus the sheet current is $J = j_c d = J_c$ there. In the nonpenetrated region ($B_z = 0$) one has $j = j_c$ near the two flat surfaces, and $j = 0$ in a current- and flux-free kernel which has approximately the shape of an ellipsoid, as assumed by Krasnov et al.,[3] but not exactly.[39] During flux penetration, the flux-
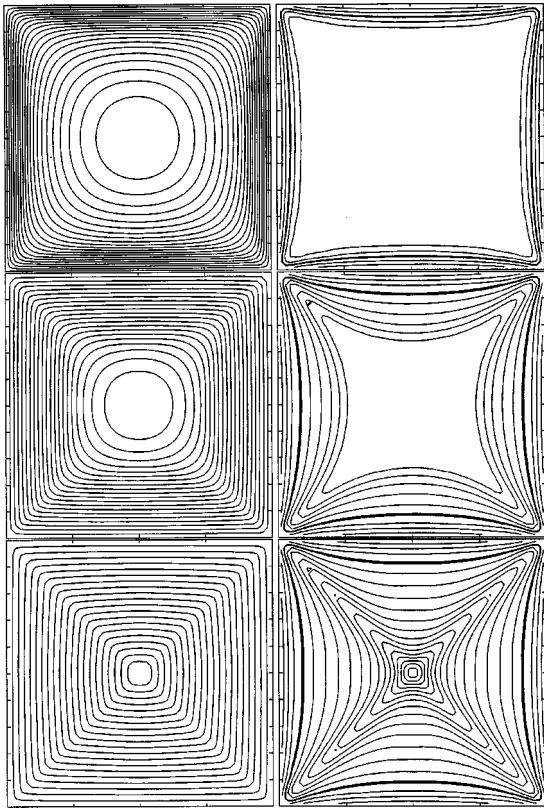
FIG. 2. The stream lines of the sheet current **J** (left) and the contour lines of the local magnetic-field component $H_z(x,y)$ perpendicular to the specimen plane (right) computed for a thin square-shaped superconductor with *isotropic* pinning. The values of the applied field H_a are $H_a = 0.25$, 0.55, and 1.55 in units of the critical sheet current J_c. The J_c value and the creep exponent $n = 19$ in the assumed law $E = E_c(J/J_c)^n$ are chosen as constants independent of $H(x,y)$, and $B = \mu_0 H$ was assumed. For this isotropic square the discontinuity lines after full penetration ($H_a \geq 1.0 J_c$) form a cross coinciding with the diagonals.

and current-free kernel initially reaches the specimen surface at the two vertices $x = y = 0$, $z = \pm d/2$, where the thickness of the two current carrying surface layers vanishes linearly, not quadratically as for the ellipsoid. When the flux front comes close to the center (distance $r \approx d/2$), the flux-free kernel starts to detach from the surface even at the two points $x = y = 0$, $z = \pm d/2$ and becomes completely isolated. The closed surface layer around the entire superconductor has now finite thickness everywhere and carries a current density of constant magnitude j_c. Near the center $x = y = 0$ one has a circulating current $\mathbf{j} = \hat{\varphi} j_c$ whose components exhibit a jump of orientation as one crosses this central line. As H_a reaches the field of full penetration the surface layer attains a thickness $d/2$ even on the line $x = y = 0$ and the flux-free kernel shrinks to a point.

The left columns in Figs. 2–5 may be interpreted in three different ways: They show (a) the contour lines of the local magnetization or current-loop density $g(x,y)$, (b) the stream lines of the current flowing in the superconducting film, and (c) they tell the intensity of the in-plane magnetic-field component $\mathbf{B}_\parallel$ at the film surface, since $\mathbf{B}_\parallel = \pm \frac{1}{2}\hat{\mathbf{z}} \times \mathbf{J}$.

The right columns in Figs. 2–5 give the contour lines of the perpendicular magnetic field $B_z(x,y)$ close to the film
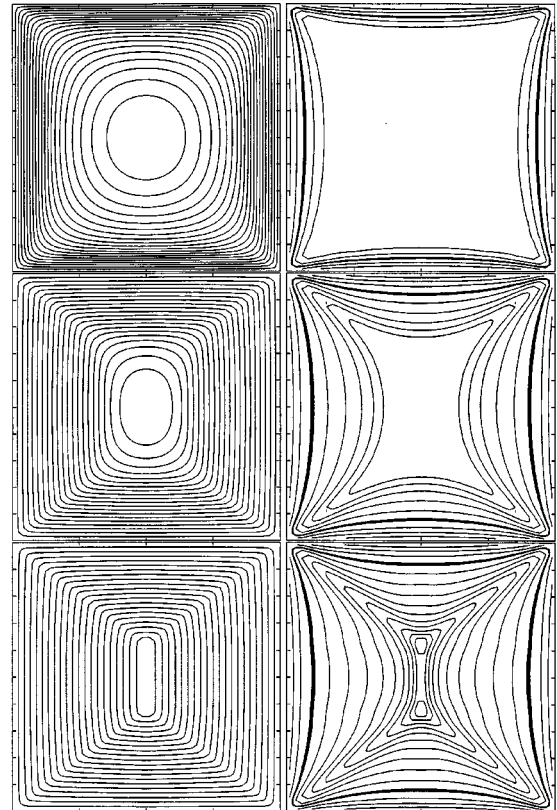

FIG. 3. As Fig. 2 but for a square with *anisotropic* critical sheet current $J_c^b/J_c^a = 1.4$. The field unit is now J_c^a. Due to the intrinsic anisotropy the discontinuity lines in the fully penetrated state ($H_a \geq 1.0 J_c^a$) form a double Y.
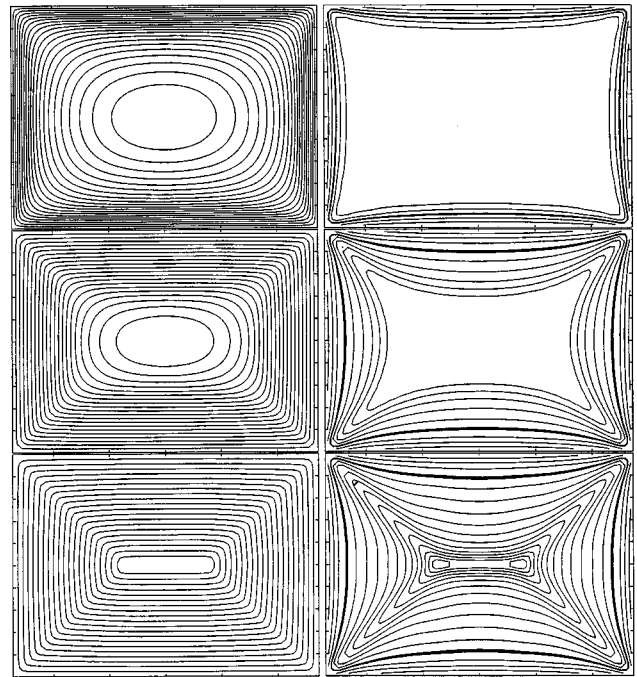

FIG. 4. As Fig. 2 but for a rectangular plate with *isotropic* pinning. The side ratio is $b/a = 1.4$. The discontinuity lines start from the corners and form an angle of 45° with the edges of the rectangle. In the fully penetrated state ($H_a \geq 1.0 J_c$) the discontinuity lines form a double Y.
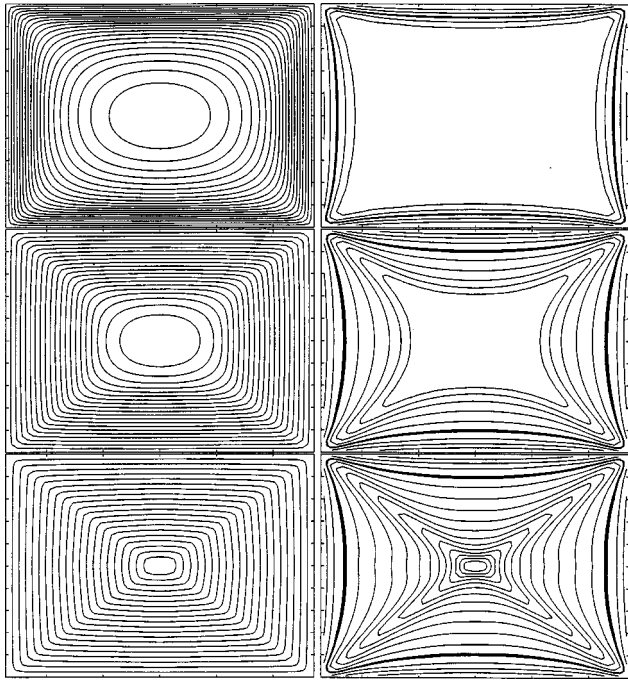
FIG. 5. As Fig. 4 but for a rectangular plate with anisotropic pinning, $J_c^b/J_c^a=b/a=1.4$. Due to the compensation of the intrinsic and shape anisotropies the discontinuity lines in the fully penetrated state ($H_a \gtrsim 1.0 J_c^a$) form a cross, like with the isotropic square.

surface. The bold line is the contour line $B_z(x,y)=B_a$. This contour line coincides with the ''neutral line'' which during flux flow in the critical state (lower row) separates the outer region where $B_z(x,y,t)$ *decreases*, from the inner region where B_z *increases*.[23]

F. Electric field

Figures 6–9 show the magnitude E of the electric field for the same isotropic and anisotropic squares and rectangles and the same H_a values as in Figs. 2–5. Note that E is induced by the moving vortex lines, thus $E=Bv$ is roughly proportional to the vortex velocity when the local induction $B=\mu_0 H$ is nearly constant. The orientation of the electric field **E** coincides with the current stream lines, and the flux-flow velocity **v** is perpendicular to **E** and **B**. Before complete flux penetration is reached, $E(x,y)$ vanishes with approximately constant slope at the cushion-shaped flux front. Inside the flux front one has $B=0$ and approximately $E=0$. More precisely, since $E\propto J^n$ and $J\propto r=(x^2+y^2)^{1/2}$ near the specimen center $r=0$, one has there $E\propto r^n$, which for $n\gg1$ is vanishingly small compared with the typical value $a\dot{B}_a$ of E near the edges.

The maximum electric field $E_{\max}$ occurs in the middle of the specimen edges. In the rectangle with isotropic pinning, this maximum is approximately the same at all four edges, $E_{\max}\approx\dot{B}_a l_p$ where $l_p=a-x_p=b-y_p\approx H_a/J_c$ is the penetration depth (see Ref. 11 for a better value of l_p). For the rectangle with anisotropic pinning, $E_{\max}$ is lower at the longer edge, along which the larger critical-current density $J_c^b=1.4J_c^a$ flows, since there the penetration depth $l_p^b\approx H_a/J_c^b$ is smaller.
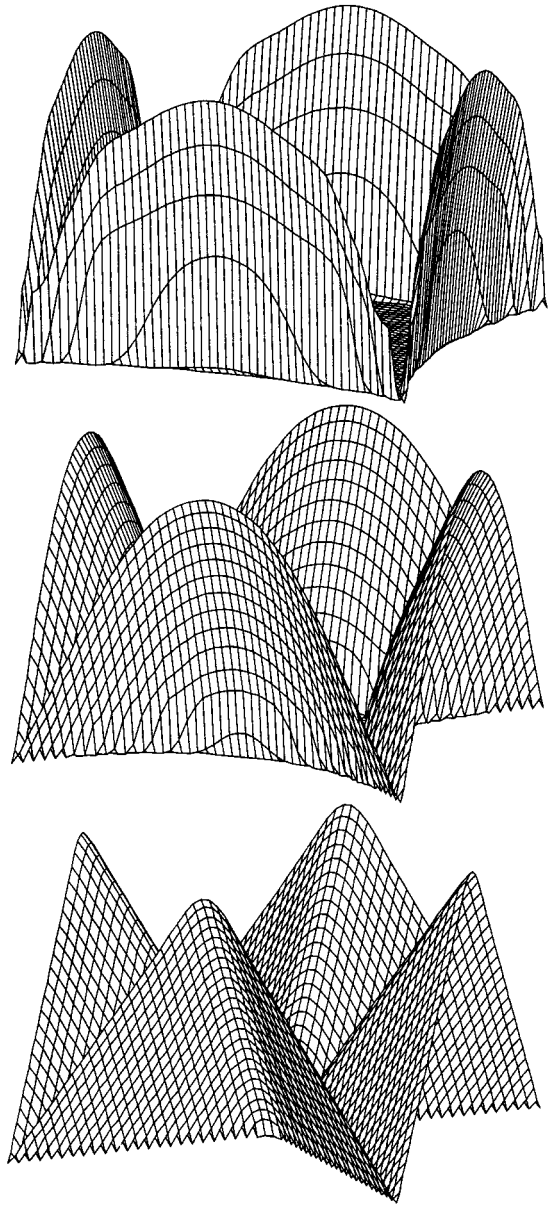

FIG. 6. The profiles of the magnitude of the electric field E during flux penetration for the isotropic square and the same H_a values as depicted in Fig. 2.

In the critical state E is an exactly linear function of x and y since the current and its self-field have saturated and are thus time independent, therefore $\nabla\times\mathbf{E}=-\dot{\mathbf{B}}=-\dot{\mathbf{B}}_a$ is constant; on the discontinuity lines one then has $E=0$ and the maximum of E is always $E_{\max}=a\dot{B}_a$ except for Fig. 9 (the anisotropic rectangle) where $E_{\max}=b\dot{B}_a$ occurs at the points $x=0$, $y=\pm b$. Since $E\propto J^n$ and $E\propto s$ where $s\ll a$ is the distance from a discontinuity line, one finds $J\propto s^{1/n}$ near all discontinuity lines. See also the discussion of $E(x,y)$ in Ref. 19.

G. Flux-flow velocity

From the flux density $B_z(x,y)$ and the magnitude of the electric field $E(x,y)$ one obtains the vortex speed $v(x,y)=|E/B_z|$. The flux flow in the specimen plane $z=0$ is
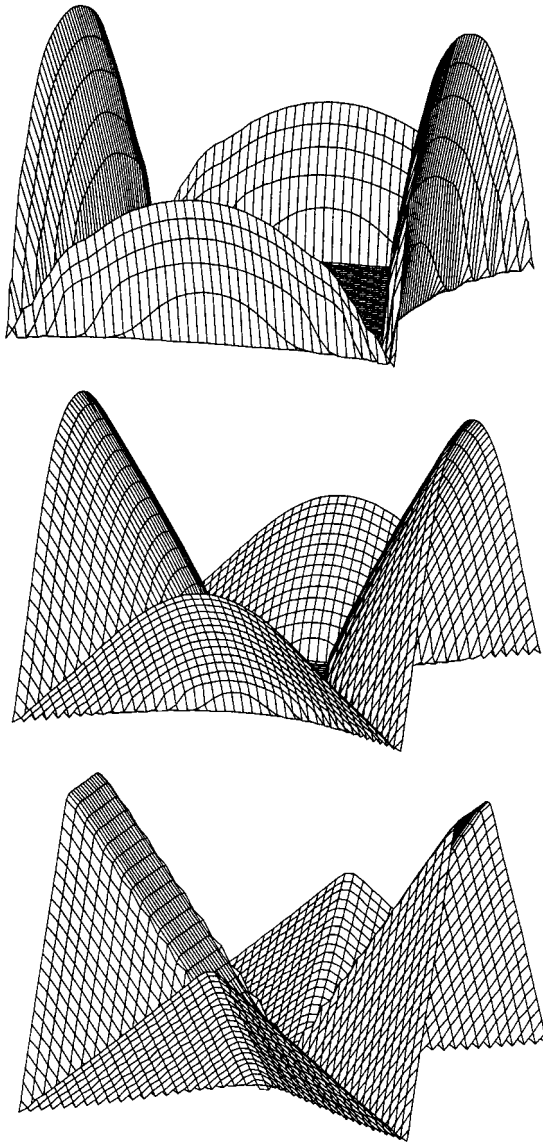
FIG. 7. The profiles of the magnitude of the electric field E during flux penetration into the anisotropic square depicted in Fig. 3.

FIG. 8. The profiles of the magnitude of the electric field E during flux penetration into the isotropic rectangle depicted in Fig. 4.

directed perpendicular to the sheet current $\mathbf{J} \| \mathbf{E} = -\mathbf{v} \times \hat{\mathbf{z}} B_z$, thus $\mathbf{v} = \mathbf{E} \times \hat{\mathbf{z}} / B_z$. The magnitude v of the flux-flow velocity during flux penetration is depicted in Fig. 10 (3D plot) and Fig. 11 (contour lines) for the isotropic and anisotropic rectangle in increasing applied field at $H_a / J_c = 0.55$ and 1.55 for the same cases depicted in Figs. 2–9. Remember that full penetration is reached when $H_a = H_p \approx J_c = j_c d$. The velocity field in the anisotropic rectangle is qualitatively similar to the electric field discussed in Sec. II F.

For incomplete penetration one has $B_z = 0$ and $E = 0$ in the nonpenetrated region; to avoid division by zero we thus used $v \approx E / (B_z + 0.03)$ (B_z in units $\mu_0 J_c$). Note in Fig. 10 that the velocity at the flux front abruptly jumps from a nearly constant value to zero, while E and B both vanish as the square root of the distance to the front. The constancy and abrupt vanishing of v means that near the flux front the vortex lattice penetrates almost as a solid. More precisely, with increasing penetration, v first increases monotonically
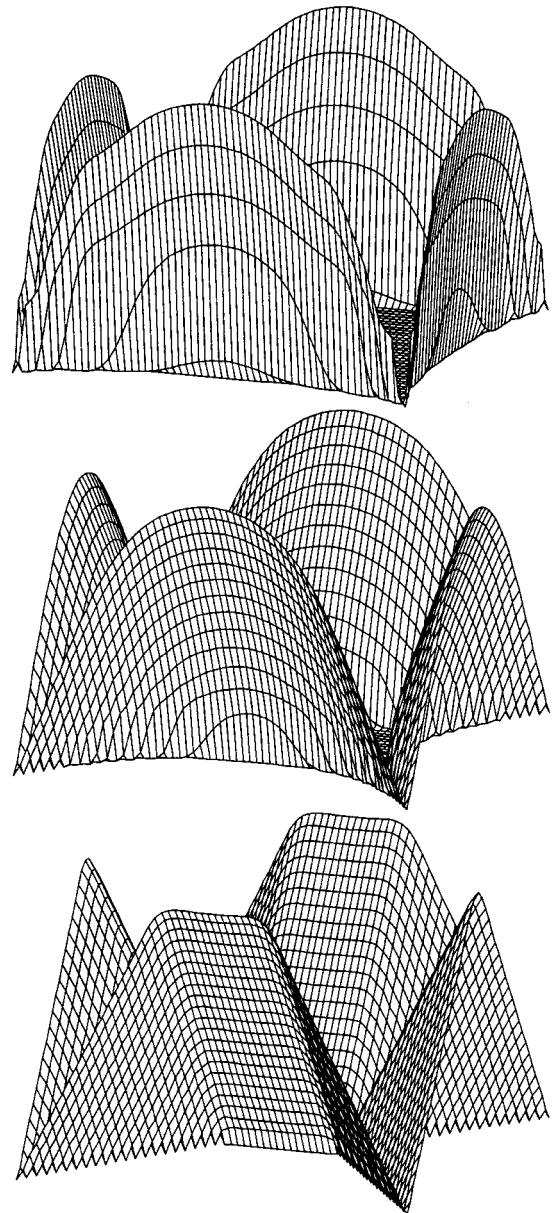
towards the flux front, but after a certain depth of order of $0.5a$, v reaches a maximum in the penetrated region and decreases towards the front.

When full penetration is reached, $H_a = H_p$, the jump in the velocity disappears and v vanishes almost linearly at the specimen center. When H_a is increased further, $B_z(x,y)$ becomes more and more constant, $B_z(x,y;H_a > H_p) = B_z(x,y;H_a = H_p) + \mu_0(H_a - H_p)$, and the velocity field looks more and more like the profiles of $|E(x,y)|$ depicted in Figs. 6–9. Therefore, $v(x,y) = |E/B|$ becomes almost linear in x and y, which means the vortex lattice is compressed nearly *uniformly* at $H_a > H_p$.

To illustrate the qualitative behavior of the speed of penetrating flux, we give the analytic expressions for a long thin superconductor strip in perpendicular H_a. The profiles of J_y, B_z, E_y, and v_x for a strip with width $2a$ and $J_c = j_c d = $ const (Bean model) look very similar to the corre-
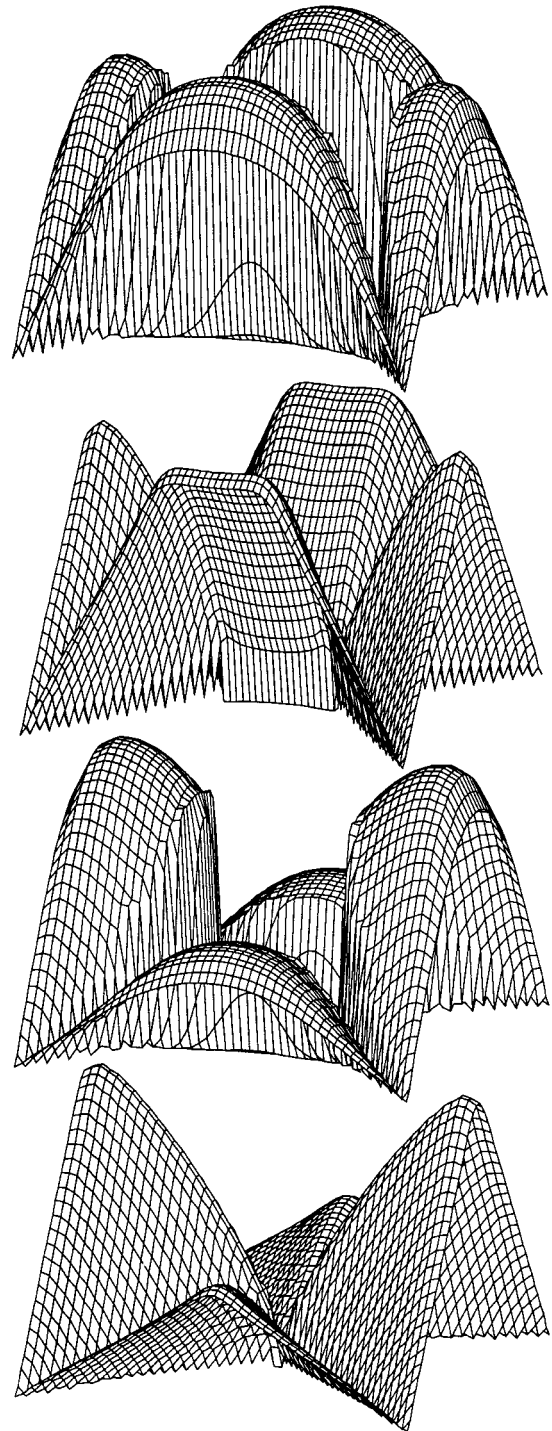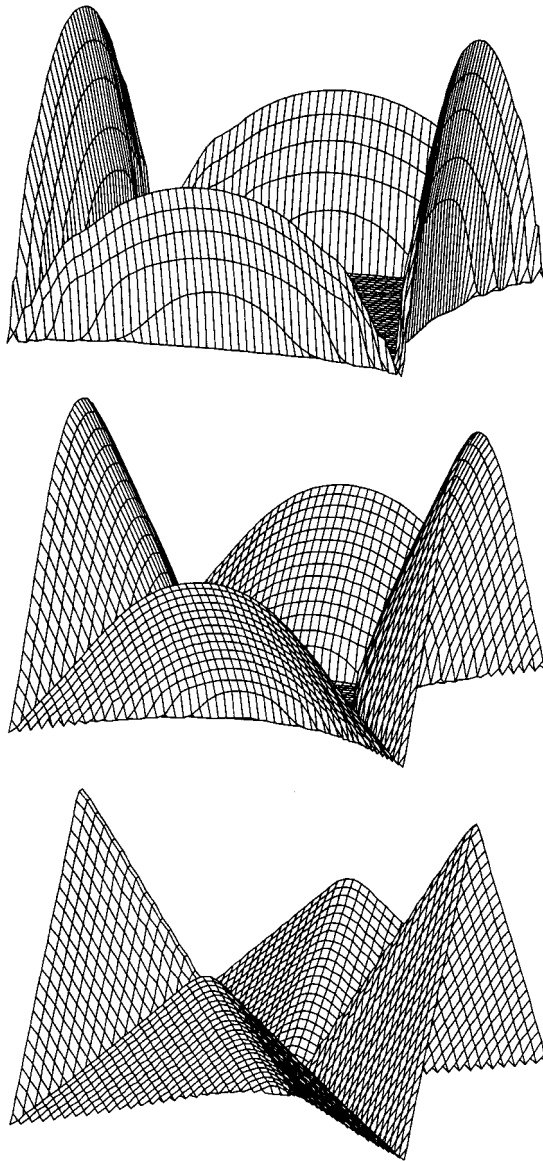
FIG. 9. The profiles of the magnitude of the electric field E during flux penetration into the anisotropic rectangle depicted in Fig. 5.

sponding profiles of a thin rectangle with $b/a \geqslant 1.4$ taken along the x axis. These profiles, measured in the specimen plane $z = 0$ (or $|z| \ll a$), are as follows:[19]

The position of the two flux fronts is $x = \pm x_p$ with $x_p = a/\cosh(\pi H_a/J_c)$, or inverted, $H_a = (J_c/\pi)\mathrm{acosh}(a/x_p)$. The vortex velocity is $v_x(x) = E_y(x)/B_z(x)$. In the nonpenetrated central zone $|x| < x_p$ one has $B_z(x) = E_y(x) = v_x(x) = 0$ and the sheet current

$$J_y(x) = -\frac{2J_c}{\pi}\mathrm{arctan}u. \tag{14}$$

In the penetrated zone $x_p \leqslant |x| \leqslant a$ the profiles are

$$J_y(x) = -J_c\mathrm{sgn}(x), \tag{15}$$

$$B_z(x) = \frac{\mu_0 J_c}{2\pi}\ln\left|\frac{1-u}{1+u}\right|, \tag{16}$$

FIG. 10. The profiles of the magnitude of the flux velocity $v = |E/B|$ during flux penetration into the isotropic (upper two plots) and anisotropic (lower two plots) rectangle depicted in Figs. 8 and 9. Shown are two values $H_a = 0.55$ and 1.55 (in units J_c). Note the abrupt jump to zero of the velocity at the flux front before complete penetration is reached.

$$E_y(x) = -\dot{B}_a(x^2 - x_p^2)^{1/2}\mathrm{sgn}(x), \tag{17}$$

$$v_x(x) = -\frac{2\pi\dot{H}_a}{J_c}\frac{(x^2 - x_p^2)^{1/2}}{\ln|(1-u)/(1+u)|}\mathrm{sgn}(x). \tag{18}$$

Here $u = cx/|x_p^2 - x^2|^{1/2}$ and $c = (1 - x_p^2/a^2)^{1/2} = \tanh(\pi H_a/J_c)$. These profiles are depicted in Fig. 12 for
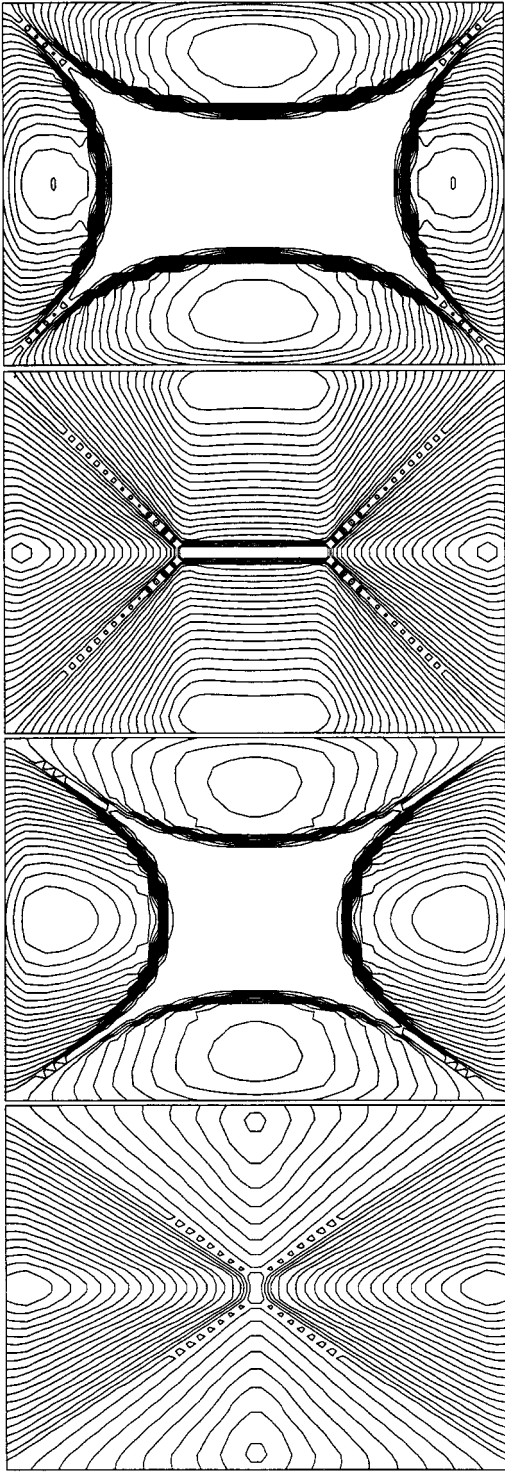
FIG. 11. The contour lines of the velocity fields depicted in Fig. 10.

FIG. 12. Magnitude of the sheet current J_y Eqs. (14) and (15), flux density B_z Eq. (16), electric field E_y Eq. (17), and flux velocity $v_x = E_y/B_z$ Eq. (18) for a thin strip of width $2a$ in increasing perpendicular field H_a. Shown are the profiles for values $H_a/J_c = 0.32$ to 7.60 (see text) corresponding to flux-front positions $x_p/a = 0.95$, 0.9, 0.8, . . . , 0.1, 0.05, 0.02, and 0.001.

$x_p/a = 0.95$, 0.9, 0.8, . . . , 0.1, 0.05, 0.02, and 0.001 corresponding to $H_a = 0.32$, 0.47, 0.69, 0.90, 1.10, 1.32, 1.57, 1.87, 2.29, 2.99, 3.69, 4.61, and 7.60. Expression (16) for $B_z(x)$ is valid also outside the specimen and exhibits the known logarithmic infinity $B_z(x) \propto \ln||x| - a|$ at the edges.

Note the nontrivial velocity profile (18): $v(x) = |v_x|$ is constant near the flux front, then goes through a maximum, and becomes nearly linear when $x_p \rightarrow 0$. This behavior is different from the velocity of the vortices in a Bean slab of same width $2a$ in *longitudinal* field H_a, which is
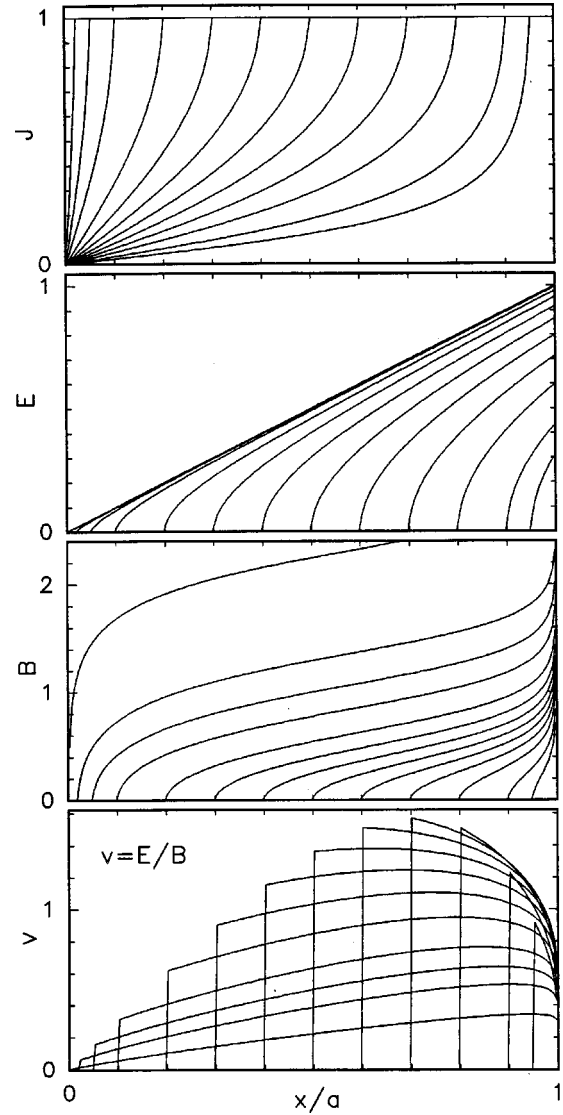
$v(x) = \dot{H}_a/j_c = $ const   for $H_a < H_p = aj_c$ and
$v(x) = (H_a/j_c)x/(x + x_0)$ with $x_0 = H_a/j_c - a > 0$ for
$H_a \geq H_p$. In particular, the velocity at the flux front $v(x_p)$ during flux penetration is constant for parallel geometry, but for perpendicular geometry $v(x_p)$ goes through a maximum and becomes zero when $H_a = H_p = (J_c/\pi)[1 + \ln(2a/d)]$ is reached. At $H_a > H_p$, the $v(x)$ in the strip is an almost linear function of x. Interestingly, if finite H_{c1} is accounted for, the profiles in parallel geometry become more similar to the profiles of the perpendicular geometry.

III. EXPERIMENTS

A. Faraday effect

We visualize the magnetic-field distribution of a superconductor by magneto-optics. Since the HTSC's themselves

have no significant magneto-optical effect, the sample surfaces have to be covered by a magneto-optically active material. For our investigations we use the magneto-optical Faraday effect. The flux penetration is imaged by detecting the rotation of the polarization plane when linearly polarized light passes a magneto-optically active layer exposed to the magnetic field of the underlying superconductor. The light is reflected from flux-free regions without rotation of the polarization plane; this light thus cannot pass an analyzer which is set in a crossed position with respect to the polarizer. In this way the Shubnikov phase (with a flux-line lattice) will be imaged as bright areas, whereas the flux-free Meissner phase remains dark. For the experiments presented in this paper we used ferrimagnetic iron-garnet films with an in-plane anisotropy as magneto-optical indicators.

The iron garnet film was grown by liquid phase epitaxy onto a gallium-gadolinium substrate with a thickness of about 3.5 μm (commercial firm Gamma Scientific Production, Russia).[40] This kind of indicator allows the flux penetration into HTSC samples to be observed directly in the whole temperature regime of superconductivity with a magnetic sensitivity of about 1 mT and a spatial resolution of about 4 μm.

The external magnetic field is generated by a copper solenoid coil, which is cooled with liquid nitrogen and produces a maximum field of 0.55 T. The observations were performed in the optical cryostat described in Refs. 41 and 42. All images can be observed directly via the microscope or be transferred to an image processing system for analyzing.[43] The image processing system allows one to determine the gray level pixel by pixel along a user-defined line.

B. Sample preparation

We use DyBa$_2$Cu$_3$O$_{7-\delta}$ (DBCO) single crystals prepared as described in Ref. 44 with dimensions of about $1000\times685\times15$ μm^3 and with $T_c\approx88$ K as measured by the Meissner effect using superconducting quantum interference device magnetometry. All crystals have a distinct twin structure, which was revealed by polarized light microscopy.

Crossed LD's were introduced by irradiation with 340-MeV Xe ions at room temperature at the ISL accelerator (Hahn-Meitner-Institut, Berlin, Germany). The samples were glued on copper sample holders and mounted at the two angles $\varphi=\pm45°$ between the ion beam and the surface normal, i.e., the c axis of the sample. The total fluence was about $\phi t=2\times10^{10}$ ions/cm^2 and the inclination direction was set parallel to the longer crystal edges. The range of the projectiles in the target material is larger than the sample thickness. The heavy-ion bombardment reduces T_c by less than 1 K at the fluence used.

C. Measured flux-density patterns

Figure 13 shows the flux distribution in a rectangular DBCO single crystal with irradiation-induced critical-current anisotropy. The sequence shows the flux penetration during increase of the perpendicular applied magnetic field from $\mu_0H_a=0$ to 41, 82, and 123 mT (from top to bottom) at temperature $T=75$ K. In these pictures the regions penetrated by the normal field component are white, while the
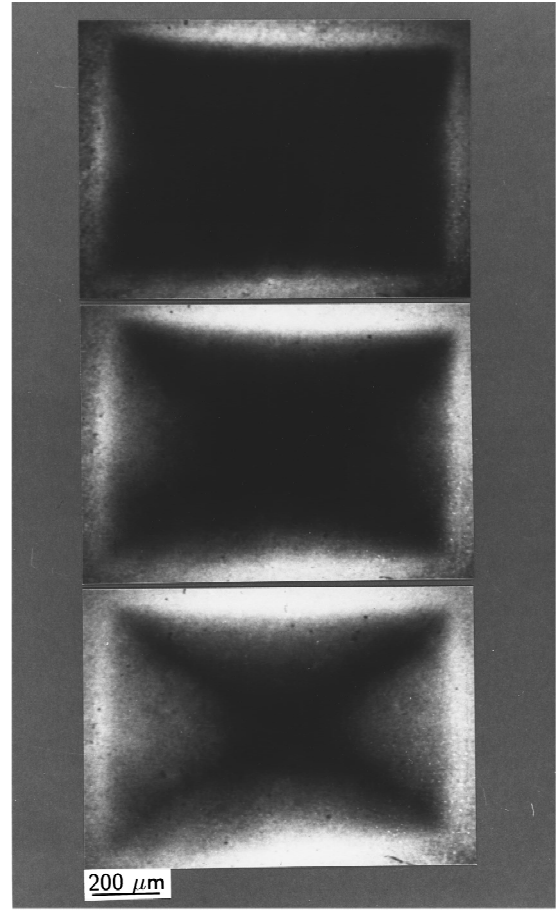

FIG. 13. Magneto-optical picture of the penetrating perpendicular flux density at the surface of a rectangular platelet of size $1000\times685\times15$ μm^3, a DBCO monocrystal with $T_c=88$ K, measured at $T=75$ K. The values of the applied field are (from top to bottom) 41, 82, and 123 mT. At this temperature the shape anisotropy 1000:685 just compensates the radiation-induced anisotropy of the critical-current density in the a-b plane. The discontinuity lines in the fully penetrated critical state thus form a cross.

flux-free Meissner phase remains dark. The measured field patterns nicely agree with the calculations shown in Fig. 5. The smaller critical current density j_c^a flows along the short sample edges, as can be seen from the faster flux penetration there. In the critical state (bottom image) the d^+ lines run along the diagonals. This means that the current anisotropy j_c^b/j_c^a exactly compensates the deviation from unity of the side ratio b/a of our rectangle, like in the calculated example.

Figure 14 shows the flux penetration into the same sample as in Fig. 13 but at lower temperature $T=60$ K ($H_a=233$ mT), where the pinning anisotropy is lower, and at higher temperature $T=80$ K ($H_a=50$ mT), where j_c^b/j_c^a is larger than at $T=75$ K. In both cases the diagonal cross which appeared at $T=75$ K after full penetration, deforms into a double Y, but the orientation of the short central line of the double Y for $T=60$ is along the longer side, like in the isotropic rectangle, but along the shorter side for $T=80$ K. At temperatures above 80 K, the anisotropy increases further but the contrast in our magneto-optical images diminishes due to decreasing penetration field H_p. At temperatures be-
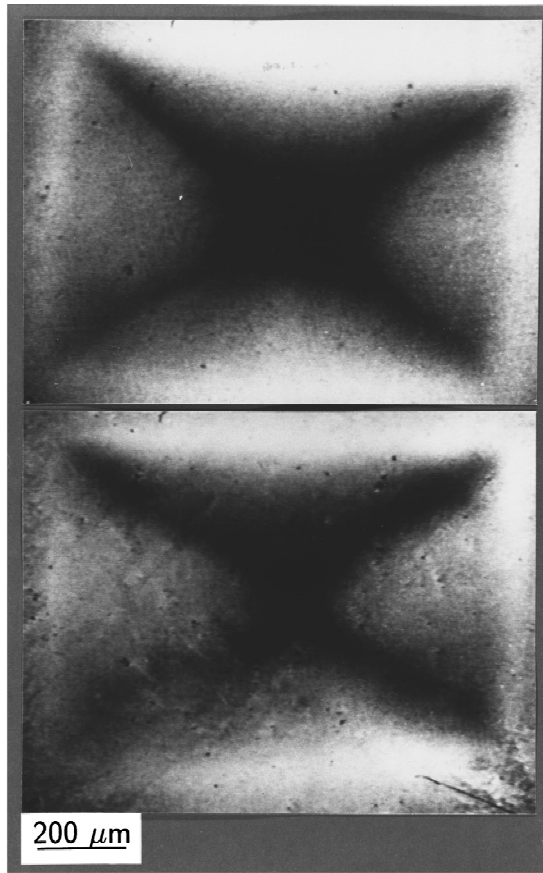
FIG. 14. The same specimen as in Fig. 13 but at lower temperature $T = 60$ K (top, $H_a = 233$ mT) and higher $T = 80$ K (bottom, $H_a = 50$ mT). At the lower $T = 60$ K, the anisotropy of the critical current density is lower; the discontinuity lines in the critical state thus form a double Y, which is located between the double Y of the isotropic rectangle and the diagonal cross of the more anisotropic rectangle shown in Figs. 5 and 10. At the higher temperature $T = 80$ K, the anisotropy of j_c is higher; the discontinuity lines in the critical state then form a double Y which is at a right angle to the double Y of the isotropic rectangle shown in Fig. 4.

low 60 K, H_p is higher than the maximum field of our experimental setup and thus the critical state is not reached.

IV. CONCLUSION

In this paper we presented patterns of electric and magnetic fields and current densities during the penetration of magnetic flux into flat type-II superconductors with an anisotropic critical-current density. Our previous numerical method to calculate currents and electric and magnetic-field patterns from first principles was extended to anisotropic critical currents for the case that these critical currents flow parallel to the sample edges. This computation method treats the superconductor as a highly nonlinear conductor with two nonlinear resistivities $\rho_{xx}(j_x)$ and $\rho_{yy}(j_y)$. The method, in principle, allows one to consider arbitrary dependences of these two resistivities on the normal field component B_z, e.g., by using creep exponents $n(B_z)$ and critical-current densities $j_c(B_z)$. Qualitative similarities between the current stream lines and the magnetic-field lines are found for the isotropic square and the anisotropic rectangle with anisotropy $j_c^a / j_c^b = a / b$, and for the isotropic rectangle and the anisotropic square.

The good agreement of the calculated field patterns with those obtained by magneto-optics on a rectangular DBCO single crystal with irradiation-induced critical-current anisotropy demonstrates the applicability of our computational method, in which anisotropic pinning is modeled by two nonlinear resistivities. In addition, we have derived the flux-flow velocity during flux penetration and discussed the qualitative differences of these velocities in parallel and perpendicular geometries.

[1] C. P. Bean, Phys. Rev. Lett. **8**, 250 (1962); Rev. Mod. Phys. **36**, 31 (1964); J. Appl. Phys. **41**, 2482 (1970).

[2] A. M. Campbell and J. E. Evetts, *Critical Currents in Superconductors* (Taylor & Francis, London, 1972).

[3] V. M. Krasnov, V. A. Larkin, and V. V. Ryazanov, Physica C **174**, 440 (1991).

[4] S. Senoussi, J. Phys. (France) III **2**, 1041 (1992).

[5] M. E. McHenry and R. A. Sutton, Prog. Mater. Sci. **38**, 159 (1994).

[6] K. V. Bhagwat and P. Chaddah, Physica C **224**, 155 (1994).

[7] Th. Schuster, M. V. Indenbom, M. R. Koblischka, H. Kuhn, and H. Kronmüller, Phys. Rev. B **49**, 3443 (1994).

[8] A. Forkl and H. Kronmüller, Physica C **228**, 1 (1994); Phys. Rev. B **52**, 16 130 (1995).

[9] H. Theuss, A. Fork, and H. Kronmüller, Physica C **190**, 345 (1992).

[10] W. T. Norris, J. Phys. D **3**, 489 (1970); Y. Young, T. Hughes, C. Beduz, D. M. Spiller, R. G. Scurlock, and W. T. Norris, Physica C **256**, 378 (1996).

[11] E. H. Brandt, M. Indenbom, and A. Forkl, Europhys. Lett. **22**, 735 (1993); E. H. Brandt and M. Indenbom, Phys. Rev. B **48**, 12 893 (1993).

[12] E. Zeldov, J. R. Clem, M. McElfresh, and M. Darwin, Phys. Rev. B **49**, 9802 (1994).

[13] P. N. Mikheenko and Yu. E. Kuzovlev, Physica C **204**, 229 (1993).

[14] J. Zhu, J. Mester, J. Lockhart, and J. Turneaure, Physica C **212**, 216 (1993).

[15] J. R. Clem and A. Sanchez, Phys. Rev. B **50**, 9355 (1994).

[16] E. Zeldov, A. I. Larkin, V. B. Geshkenbein, M. Konczykowski, D. Majer, B. Khaykovich, V. M. Vinokur, and H. Shtrikman, Phys. Rev. Lett. **73**, 1428 (1994); E. Zeldov *et al.*, Physica C **235-240**, 2761 (1994); N. Morozov, E. Zeldov, D. Majer, and B. Khaykovich, Phys. Rev. Lett. **76**, 138 (1996); I. L. Maksimov and A. A. Elistratov, Pis'ma Zh. Éksp. Teor. Fiz. **61**, 204 (1995) [JETP Lett. **61**, 208 (1995)].

[17] M. Benkraouda and J. R. Clem, Phys. Rev. B **53**, 5716 (1996); J. R. Clem, R. P. Huebener, and D. E. Gallus, J. Low Temp. Phys. **5**, 449 (1973); W. Buck, K.-P. Selig, and J. Parisi, *ibid.* **45**, 21 (1981); J. Provost, E. Paumier, and A. Fortini, J. Phys. F **4**, 439 (1974).

[18] E. H. Brandt, Phys. Rev. Lett. **74**, 3025 (1995).

[19] E. H. Brandt, Phys. Rev. B **52**, 15 442 (1995).

[20] E. H. Brandt, Rep. Prog. Phys. **58**, 1465 (1995).

[21] Th. Schuster, M. V. Indenbom, H. Kuhn, E. H. Brandt, and M. Konczykowski, Phys. Rev. Lett. **73**, 1424 (1994).

[22] Th. Schuster, H. Kuhn, E. H. Brandt, M. Indenbom, M. R. Koblischka, and M. Konczykowski, Phys. Rev. B **50**, 16 684 (1994).

[23] Th. Schuster, H. Kuhn, and E. H. Brandt, Phys. Rev. B **51**, 697 (1995).

[24] Th. Schuster, H. Kuhn, E. H. Brandt, M. V. Indenbom, M. Kläser, G. Müller-Vogt, H.-U. Habermeier, H. Kronmüller, and A. Forkl, Phys. Rev. B **52**, 10 375 (1995).

[25] Th. Schuster, H. Kuhn, and E. H. Brandt, Phys. Rev. B **54**, 3514 (1996).

[26] Th. Schuster, M. V. Indenbom, H. Kuhn, H. Kronmüller, M. Leghissa, and G. Kreiselmeyer, Phys. Rev. B **50**, 9499 (1994).

[27] Th. Schuster, H. Kuhn, M. Indenbom, M. Leghissa, M. Kraus, and M. Konczykowski, Phys. Rev. B **51**, 16 358 (1995).

[28] Th. Schuster, M. R. Koblischka, H. Kuhn, M. Glücker, B. Lude-

scher, and H. Kronmüller, J. Appl. Phys. **74**, 3307 (1993).

[29] C. A. Durán, P. L. Gammel, R. Wolfe, V. J. Fratello, D. J. Bishop, T. Kimura, K. Kitazawa, and K. Kishio, Phys. Rev. B **49**, 3608 (1994).

[30] E. Cuche, M. V. Indenbom, M.-O. André, P. Richard, W. Benoit, and Th. Wolf, Physica C **256**, 324 (1996).

[31] H. A. M. van den Berg, J. Appl. Phys. **60**, 1104 (1986).

[32] Th. Schuster, H. Kuhn, and M. Indenbom, Phys. Rev. B **52**, 15 621 (1995).

[33] A. Gurevich, Phys. Rev. Lett. **65**, 3197 (1990).

[34] A. Gurevich, Phys. Rev. B **46**, 3638 (1992); Supercond. Sci. Technol. **5**, 383 (1992).

[35] E. H. Brandt, Phys. Rev. B **46**, 8628 (1992).

[36] P. D. Grant, M. W. Denhoff, W. Xing, P. Brown, S. Govorkov, J. C. Irwin, B. Heinrich, H. Zhou, A. A. Fife, and A. R. Cragg, Physica C **229**, 289 (1994).

[37] W. Xing, B. Heinrich, Hu Zhou, A. A. Fife, and A. R. Cragg, J. Appl. Phys. **76**, 4244 (1994).

[38] E. H. Brandt, Phys. Rev. B **55**, 14 513 (1997).

[39] E. H. Brandt, Phys. Rev. B **54**, 4246 (1996).

[40] L. A. Dorosinskii, M. V. Indenbom, V. I. Nikitenko, Yu. A. Ossip'yan, A. A. Polyanskii, and V. K. Vlasko-Vlasov, Physica B **203**, 149 (1992).

[41] Th. Schuster, M. R. Koblischka, N. Moser, B. Ludescher, and H. Kronmüller, Cryogenics **31**, 811 (1991).

[42] K.-H. Greubel, E. Gmelin, N. Moser, Ch. Mensing, and L. Walz, Cryogenics **30**, (Suppl.), 457 (1990).

[43] M. R. Koblischka, N. Moser, B. Gegenheimer, and H. Kronmüller, Physica C **166**, 36 (1990).

[44] C. Thomsen, M. Cardona, B. Gegenheimer, R. Liu, and A. Simon, Phys. Rev. B **37**, 9860 (1988).

[45] A. Forkl, Phys. Scr. **T49**, 148 (1993).